GSCE Faculty Publications   Geospatial Sciences Center of Excellence (GSCE)

8-2016

A Comparison of Tropical Rainforest Phenology Retrieved From Geostationary (SEVIRI) and Polar-Orbiting (MODIS) Sensors Across the Congo Basin

Dong Yan
South Dakota State University, dong.yan@sdstate.edu

Xiaoyang Zhang
South Dakota State University, xiaoyang.zhang@sdstate.edu

Yunyue Yu
NOAA, National Environmental Satellite, Data, and Information Service, Center for Satellite Applications and Research (STAR)

Wei Guo
NOAA, National Environmental Satellite, Data, and Information Service, Center for Satellite Applications and Research (STAR)

Recommended Citation

A Comparison of Tropical Rainforest Phenology Retrieved From Geostationary (SEVIRI) and Polar-Orbiting (MODIS) Sensors Across the Congo Basin

Dong Yan, Xiaoyang Zhang, Yunyue Yu, and Wei Guo

Abstract—The seasonal and interannual dynamics of tropical rainforests play a critical role in the global carbon cycle and climate change. This paper retrieved and compared land surface phenology from observations acquired by the Spinning Enhanced Visible and Infrared Imager (SEVIRI) onboard geostationary satellites and the Moderate Resolution Imaging Spectroradiometer (MODIS) on polar-orbiting satellites over the Congo Basin. To achieve this, we first retrieved canopy greenness cycles (CGCs) and their transition timing from two-band enhanced vegetation index (EVI2) derived from SEVIRI and MODIS data between 2006 and 2013. We then assessed the influences of SEVIRI and MODIS data quality on the reconstruction of the EVI2 temporal trajectory, the detection of the CGC onset and end timing, and the total number of successful CGC retrievals. The significance of influences was determined using the one-tailed two-sample Kolmogorov–Smirnov test. The results indicate that diurnal SEVIRI observations greatly increased the probability of capturing cloud-free daily EVI2 in the rainforest-dominated region of the Congo Basin, where the proportion of good quality (PGQ) observations during a CGC was up to 80% higher than that from MODIS. As a result, the double annual CGCs of the Congo Basin rainforests were well identified from SEVIRI but sparsely detected from MODIS, whereas the single annual CGC in the savanna-dominated northern and southern Congo Basin was successfully retrieved from both SEVIRI and MODIS. Moreover, the decreases of PGQ in an EVI2 time series were found to significantly increase the uncertainties of retrieved phenological timings and increase the probabilities of CGC retrieval failures.

Index Terms—Congo basin, Moderate Resolution Imaging Spectroradiometer (MODIS), Spinning Enhanced Visible and Infrared Imager (SEVIRI), tropical rainforest phenology.

D. Yan and X. Zhang are with the Geospatial Sciences Center of Excellence, South Dakota State University, Brookings, SD 57007 USA (e-mail: dong.yan@sdstate.edu; xiaoyang.zhang@sdstate.edu).

Y. Yu is with the National Oceanic and Atmospheric Administration, National Environmental Satellite, Data, and Information Service, Center for Satellite Applications and Research (STAR), Camp Springs, MD 20746 USA (e-mail: yunyue.yu@noaa.gov).

W. Guo is with the I. M. Systems Group, National Oceanic and Atmospheric Administration, National Environmental Satellite, Data, and Information Service, Center for Satellite Applications and Research (STAR), College Park, MD 20740 USA (e-mail: wei.guo@noaa.gov).

I. INTRODUCTION

THE Congo Basin rainforest has a coverage of 180 million hectares, which accounts for about 90% of the rainforests in Africa and one-third of the world's tropical rainforests and represents the second largest rainforest block on Earth [1]–[3]. Compared with the rainforests in the Amazon Basin and Southeast Asia, the Congo Basin rainforest has experienced significantly less anthropogenic deforestation and represents the only intact rainforest in the world [4]. Carbon storage in the global tropical rainforests accounts for about 40%–50% of the total carbon in terrestrial vegetation, and the Congo Basin rainforest is therefore a critical component of this huge carbon pool [2]. Changes in the productivity of the Congo Basin rainforest can impose strong influences on the global carbon cycle [2], [5]. It is, however, challenging to model changes in the productivity of the Congo Basin rainforest with the scarce knowledge of rainforest phenology in this region [6], [7]. The challenges in understanding rainforest phenology in the Congo Basin are twofold. On the one hand, rainforest trees have complex behaviors in leaf and reproductive phenology, which vary across forest layers and between and within species [5], [6], [8]. For example, the deciduousness of rainforest trees is found to decrease toward the lower layers of rainforests [6], and the leaf-exchange process is asynchronous within a rainforest tree community [7]. On the other hand, the civil conflicts in the Congo Basin make it very difficult to acquire *in situ* observations [1]. Therefore, long-term studies on rainforest phenology based on *in situ* observations in the Congo Basin are rarely seen [6].

Remote sensing represents an alternative way to acquire long-term phenological observations of the Congo Basin rainforest. Instead of providing phenological observation for tree individuals, remotely sensed photosynthetically active radiation has been used to retrieve land surface phenology (LSP), which refers to the seasonal variations in canopy greenness over vegetated land surfaces [9], [10]. Although long-term LSP products for Africa have been developed based on observations from polar-orbiting sensors such as the Advanced Very High Resolution Radiometer (AVHRR) [11] and the Moderate Resolution Imaging Spectroradiometer (MODIS) [12], the rainforest-dominated region in the Congo Basin remains a gap in those products due to the prolonged duration of cloud cover. By compositing cloud-free observations from multiple years,
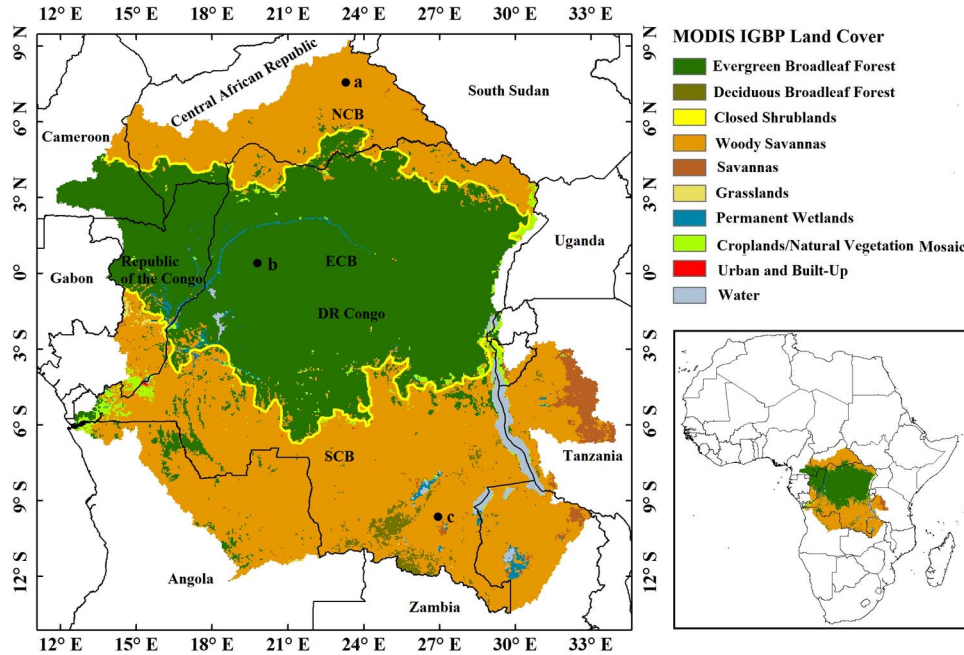
Fig. 1. Distribution of land cover within the Congo Basin extracted from the MODIS IGBP land cover product. Black lines represent the country boundaries, and yellow lines are the boundaries between the NCB, ECB, and SCB. The boundary of the Congo Basin represents the watershed boundary of the Congo River, and it is downloadable at http://www.arcgis.com/home/item.html?id=701ea1a7435d4c70b2d7bae9e77ae0bc. Black dots represent the three randomly selected pixel locations.

the climatological LSP for the Congo Basin rainforest has finally been generated from polar-orbiting sensors in recent studies [7], [13], [14]. However, the interannual variations in LSP remain poorly understood.

The sensors carried by geostationary satellites have the capability to make frequent diurnal observations. This allows us to obtain a larger number of daily cloud-free observations relative to polar-orbiting sensors for a fixed location, which is particularly important for monitoring LSP in cloud-prone regions [15], [16]. For example, it has been demonstrated that the shortest compositing period to acquire a cloud-free image across the cloud-prone West Africa increases from only three days for the Spinning Enhanced Visible and Infrared Imager (SEVIRI) onboard the Meteosat Second Generation (MSG) series of geostationary satellites to 16 days for AVHRR and MODIS [15]. The interannual variations in rainforest LSP between 2007 and 2011 across the Congo Basin has been successfully retrieved using the SEVIRI-derived leaf area index [17] and normalized difference vegetation index [18].

It is worth noting that the advantage of retrieving LSP from MODIS observations lies in the finer spatial resolution that MODIS offers compared to that by SEVIRI (250–500 m for MODIS versus 3–5 km for SEVIRI) [7], [13]. It is therefore interesting to compare the LSP retrievals from MODIS and SEVIRI data and to conduct an assessment of the influences of cloud cover on the differences in the retrieved rainforest LSP. The assessment can provide us an understanding of the quantified uncertainties in the retrieved LSP from MODIS, which would benefit the fusion of LSP products from MODIS and SEVIRI for a better LSP monitoring of the Congo Basin rainforest. To the best of our knowledge, there have been only two previous studies on the differences in the retrieved LSP from MODIS and SEVIRI in the Congo Basin [17], [18].

However, the rainforest-dominated region was excluded from the analyses in one study [17], whereas the other study focuses on the influences of LSP retrieval algorithms (the modified iterative interpolation for data reconstruction versus the double logistic curve fitting) rather than on the influences imposed by cloud cover [18].

This paper aims to compare LSP retrievals from SEVIRI and MODIS observations across the Congo Basin and then to assess the influences of cloud cover on LSP retrievals. To this end, we first generated daily two-band enhanced vegetation index (EVI2) time series between 2006 and 2013 from SEVIRI and MODIS data. The time series of EVI2 was then used to retrieve LSP using the hybrid piecewise logistic model (HPLM). The quality of time series of SEVIRI EVI2 and MODIS EVI2 was further quantified, and the impacts of data quality on LSP retrievals were finally examined.

II. BACKGROUND

The Congo Basin was divided into three subbasins based on the 0.05° MODIS land cover product [19] to better describe LSP across different ecosystems and articulate the influences of data quality on LSP retrievals (see Fig. 1). The northern Congo Basin (NCB) (roughly between 3° N and 9° N) is dominated by woody savannas. The equatorial Congo Basin (ECB) (roughly between 6° N and 6° S) is occupied by evergreen broadleaf forests. The southern Congo Basin (SCB) (roughly between 0° and 12° S) primarily consists of woody savannas, in which isolated patches of evergreen broadleaf forests, savannas, deciduous broadleaf forests, and cropland/natural vegetation mosaics exist.

LSP characterizes canopy greenness cycles (CGCs) retrieved from remotely sensed data. It is commonly used to describe the

vegetation growing season or cycle from green leaf appearances to leaf abscissions at canopy level [9], [10], [20], [21]. Instead of exhibiting completely dormant phases, tropical rainforests present gradual variations in seasonal leaves with the simultaneous reduction of old leaves and increase of new leaves [6]. To more precisely characterize LSP across the Congo Basin, we used "CGC" to term the seasonal greenness variation determined from the EVI2 time series.

Previous studies have shown that tropical rainforests in the Congo Basin have two CGCs during a year, whereas other types of land cover only have a single annual CGC [13], [14], [17]. In this paper, we referred to the CGC initiated before and after July as CGC in the first and second cycles, respectively. Specifically, the first CGC primarily occurs in ECB and NCB which coincides with the rainy season regulated by the northward movement of the Intertropical Convergence Zone (ITCZ) [13]. The second CGC mainly occur within ECB and SCB when the rainy season controlled by the southward movement of ITCZ begins to unfold [13].

III. DATA AND METHODS

A. Generation of SEVIRI and MODIS Three-Day EVI2 Time Series

SEVIRI onboard the MSG geostationary satellites (i.e., MSG-8, MSG-9, MSG-10, and MSG-11) is positioned at a fixed location of $0°$ N and $0°$ E. It is able to make a full disk scan every 15 min, covering Africa, Europe, and the northeast corner of South America. Across the Congo Basin, the pixel size of the SEVIRI observation increases from the west ($\sim 3 \times 3$ km) to the east ($\sim 5 \times 5$ km) due to the increases in the satellite zenith angle from approximately $20°$ at $13°$ E to about $40°$ at $30°$ E [22].

We collected 30-min radiances of SEVIRI red and near-infrared channels between 2005 and 2014, which were then converted to top-of-atmosphere reflectances [23]. A cloud mask for each 30-min observation was generated based on a Bayesian approach [24]. EVI2 was calculated using [25]

$$\text{EVI2} = 2.5 \frac{(\text{NIR} - \text{RED})}{(\text{NIR} + 2.4\,\text{RED} + 1)}. \tag{1}$$

In (1), NIR and RED are the 30-min red and near-infrared reflectances, respectively.

Note that we calculated EVI2 instead of the commonly used enhanced vegetation index (EVI) [26]. This is because SEVIRI does not have a blue channel (e.g., 0.45–0.51 μm), which is needed to derive EVI. EVI2 has similar performances to EVI in terms of vegetation monitoring [25], and it outperforms NDVI with increased sensitivity in densely vegetated regions [25] and reduced sensitivity to soil backgrounds [27]. In order to eliminate the variations in EVI2 caused by the varying sun–satellite geometry, we generated a daily angularly corrected EVI2 time series using the empirical kernel-driven model (2) developed for SEVIRI in a previous study [28]

$$\text{EVI2}(\theta_{t0}, \delta_{t0}, \phi_{t0})$$
$$= \text{EVI2}(\theta_{t1}, \delta_{t1}, \phi_{t1}) \frac{(1 + C_0 \text{FS}_{t0} + C_1 \text{FR}_{t0})}{(1 + C_0 \text{FS}_{t1} + C_1 \text{FR}_{t1})}. \tag{2}$$

In (2), $\text{EVI2}(\theta_{t0}, \delta_{t0}, \phi_{t0})$ is the modeled EVI2 under a reference sun–satellite geometry ($\theta_{t0} = 45°$, $\delta_{t0} = 45°$, $\phi_{t0} = 90°$), in which θ is the solar zenith angle, δ is the satellite zenith angle, and ϕ is the sun–satellite relative azimuth angle. $\text{EVI2}(\theta_{t1}, \delta_{t1}, \phi_{t1})$ is the observed EVI2 at time $t1$. C_0, and C_1 are kernel weights, which are -0.0723 and -0.0101 for SEVIRI, respectively [28]. FS and FR represent the kernel function that models the changes in EVI2 caused by those in the solar and satellite zenith angles and the sun–satellite relative azimuth angle, respectively [28]. For time $t = t0$ or $t1$

$$FS_t = \tan \theta_t + \tan \delta_t \tag{3}$$

$$FR_t = (\cos \phi_t + 1)^2 (\tan \theta_t + \tan \delta_t)^{\frac{1}{2}}. \tag{4}$$

EVI2 in each 30-min observation was first converted to an EVI2 acquired under the reference sun–satellite geometry using (2). Daily angularly corrected EVI2 was then determined as the maximum angularly corrected 30-min EVI2 obtained within a day with solar and satellite zenith angles being less than $60°$. The daily angularly corrected EVI2 was further composited into a three-day EVI2 time series between 2005 and 2014 by determining the maximum EVI2 acquired under cloud-free conditions. As a result, there were 122 three-day EVI2 composites in each year. Each three-day SEVIRI EVI2 composite was assigned one of the following quality assurance (QA) flags: 0—clear, 1—cloudy, 2—bad input (i.e., solar zenith angle $>= 60°$ or satellite zenith angle $>= 60°$), and 3—water.

We also obtained polar-orbiting satellite data for LSP retrievals. To match the spatial resolution of SEVIRI (i.e., $\sim$3–5 km), we selected the MODIS daily surface reflectance product (MOD09CMG collection 5: https://lpdaac.usgs.gov/products/modis_products_table/mod09cmg) with a $0.05°$ resolution (~ 5 km) between 2005 and 2014. The MOD09CMG surface reflectance product was generated based on data acquired by the MODIS sensor onboard Terra, and it has been corrected for angular effects using a model that has been optimized for vegetation monitoring purposes based on tailored angular correction coefficients for different biomes [29]. In this paper, we chose to only use the surface reflectance product from Terra instead of combining it with that from Aqua (MYD09CMG) due to the following two concerns. First, the diurnal variation of cloud cover during the rainy season in central Africa has been reported as increasing convective clouds from morning to the afternoon [13], which limits the chances that the MYD09CMG product could increase the amounts of cloud-free observations. Second, the MODIS angular correction model is less effective in cloud-persistent regions (e.g., the tropical and high-latitude areas) than in other parts of the world [29]. A simple combination of surface reflectance data from Terra and Aqua would likely increases the noises in MODIS time series due to the inconsistent sun–satellite geometries.

The MODIS daily EVI2 was further calculated using (1), which was then composited into a three-day EVI2 time series in the same manner as that of SEVIRI EVI2. QA flags for MODIS three-day EVI2 composites are as follows: 0—clear, 1—snow, 2—partially cloudy, 3—cloud shadow, 4—not set, assumed clear, 8—cloudy, 9— no observation, and 10—water. To simplify the QA flags in LSP retrievals, we grouped the QA

flags of "partially cloudy," "cloud shadow," and "cloudy" as "cloudy" and the QA flags of "clear" and "assumed clear" as "clear."

To compare SEVIRI EVI2 with MODIS EVI2 within the same spatial reference system, we resampled the three-day SEVIRI EVI2 composites to a spatial resolution of 0.05°. For each 0.05° grid, the SEVIRI pixels that fell within it were classified into four categories based on QA flags: clear, cloudy, bad input, and water. EVI2 for each 0.05° grid was then determined based on the mean EVI2 from the majority category (i.e., the category containing the highest number of pixels), if the majority category was either clear sky condition or cloud contamination. A fill value of -9999 was assigned to the 0.05° grid if the majority category was either bad input or water.

B. Detection of LSP From SEVIRI and MODIS Data and Investigation of LSP Differences

LSP was retrieved from the 0.05° three-day SEVIRI and MODIS EVI2 time series using the HPLM-based LSP detection algorithm (HPLM-LSPD) during 2006–2013. The HPLM-LSPD was applied based on the following five steps [30]. (1) For each year between 2006 and 2013, we prepared a three-day EVI2 time series with a total of 244 three-day EVI2 composites which comprised the 61 composites from the latter half of the preceding year, the 122 composites of the target year, and the 61 composites from the earlier half of the succeeding year. (2) Background EVI2 was calculated as the average of the five largest good quality EVI2 during a dormancy period. In the context of this study, the dormancy period should be interpreted as the time period between two consecutive CGCs, which roughly corresponds to a dry season in the Congo Basin. (3) The three-day EVI2 time series was smoothed by removing spuriously high value filling gaps caused by atmospheric contaminations using nearest good quality observations, and filtering irregular values using the Savitzky–Golay filter and a local median filter. (4) The EVI2 temporal trajectory was then reconstructed by fitting logistic curves to the smoothed EVI2 time series using HPLM. (5) The timing of the CGC onset and end was defined as the day when an EVI2 temporal trajectory exhibited the maximum rate of change in curvature during the ascending and descending phases, respectively [10]. The HPLM-LSPD has two assumptions. First, the reconstructed EVI2 trajectory should not fall below the background EVI2 during a dormancy period. Second, the duration of the dormancy period is at least one month.

The mean onsets and ends of CGC were calculated for each 0.05° grid where the CGC onset and end were detected in at least four years between 2006 and 2013. To illustrate the overall spatial pattern of LSP shifts across the Congo Basin, we further computed the latitudinal averages of the mean CGC onset and end derived from SEVIRI and MODIS EVI2s. The latitudinal averages were calculated for each 0.05° interval between 8° N and 12° S following the method developed by a previous study [31]. Specifically, we first identified a 60-day window containing the maximum number of grids with CGC onsets, which trimmed the irregular values in the distribution. We then computed the mean value of CGC onsets within the selected 60-day window, which represented the latitudinal average. The latitudinal average in mean CGC end was derived in the same manner.

To better illustrate how SEVIRI and MODIS observations were used in LSP retrievals, the original and reconstructed EVI2 temporal trajectories in three pixel-based samples were examined. These samples were randomly selected from woody savannas in NCB and SCB and evergreen broadleaf forests in ECB (sample locations are provided in Fig. 1). Specifically, we compared the mean and standard deviation in CGC timing, CGC duration, EVI2 amplitude, and ratio of EVI2 amplitude to peak EVI2 during a CGC from 2006 to 2013.

We investigated the absolute differences between SEVIRI and MODIS LSP retrievals on a per-pixel basis and across the three subbasins (NCB, ECB, and SCB), respectively. On a per-pixel basis, we calculated the absolute differences in the timing of the CGC onset and end during the first and second cycles in each year and further examined the mean value and the standard deviation of the absolute differences between 2006 and 2013. Similarly, we calculated the differences in the total number of successful CGC retrievals from SEVIRI and MODIS data. This calculation was carried out separately for the first and the second CGC on a per-pixel basis. In order to characterize and quantify the difference in CGC retrieval at the subbasin scale, we calculated the proportions of pixels where the CGC onset and end were detected within a year from SEVIRI and MODIS data in NCB, ECB, and SCB, respectively, which was considered as the CGC detection rate in a subbasin. In ECB, we determined the CGC detection rate as the proportion of pixels where both the CGC onset and end were successfully detected twice in a year.

C. Evaluation of the Reconstructed SEVIRI and MODIS EVI2 Temporal Trajectories

We computed two indices to evaluate the qualities of the original and reconstructed EVI2 temporal trajectories during a CGC. This is because it has been shown that EVI2 obtained outside a CGC does not affect the retrieval of the seasonal dynamics in canopy greenness [16]. The first index is the proportion of good quality observations (i.e., cloud-free observations) (PGQ) during a CGC, which was calculated using a moving-window-based methodology [30]. We counted the total number of three-day EVI2 composites within a CGC and denoted it as T. Based on the QA flags of SEVIRI and MODIS data, the number of good quality observations (NGQ) was then counted using a nine-day moving window, which began at the onset of CGC and continued until the end of CGC with a step length of three days. A good quality observation was added to NGQ as long as there was one cloud-free observation within the nine-day moving window. The size of the moving window was determined according to the finding that a reliable EVI2 temporal trajectory could be established using the HPLM as long as one good quality observation could be obtained every eight days [16]. PGQ was finally calculated as NGQ divided by T. The moving-window-based PGQ has been reported as an objective measurement of data quality for LSP retrieval purposes [30].

The second index is the fit quality index (FQI) of the reconstructed EVI2 temporal trajectories within a CGC, which

was calculated using [30]

$$FQI = \left(1 - \frac{\sum_{i=1}^{N}(M_i - O_i)^2}{\sum_{i=1}^{N}\left(|M_i - \overline{O}| + |O_i - \overline{O}|\right)^2}\right) \times 100\%. \quad (5)$$

In (5), N is the total NGQ within a CGC, and O_i and M_i represent the ith original good quality EVI2 and the corresponding HPLM-modeled EVI2, respectively. $\overline{O}$ is the mean of the original EVI2 with good quality. FQI measures the overall similarity between the original EVI2 with good quality and the corresponding HPLM-reconstructed EVI2 within a CGC. The FQI value of 0% represents the lowest degree of similarity between the original and the reconstructed EVI2, whereas 100% indicates that the original and reconstructed EVI2 values are the same [30]. We then investigated the differences in PGQ and FQI between SEVIRI and MODIS EVI2 time series. Specifically, for each 0.05° pixel, we calculated the absolute differences in PGQ and FQI during each year. We further calculated the mean value and the standard deviation of the absolute differences from 2006 to 2013.

D. Assessment of the Data Quality Influence on EVI2 Trajectory Reconstruction and LSP Retrieval

PGQ in an EVI2 time series was hypothesized to have significant influences on the reconstruction of the EVI2 temporal trajectory and the retrieval of LSP. The influences could be assessed by comparing CGC parameters retrieved from SEVIRI and MODIS data. Therefore, we investigated the influences by comparing the absolute differences in PGQ between the original SEVIRI and MODIS EVI2 time series with the absolute differences in the following: 1) FQI of the reconstructed EVI2 temporal trajectories; 2) the retrieved CGC onset timing; 3) the retrieved CGC end timing; and 4) the total number of successful CGC retrievals from 2006 to 2013. Since the four analyses were conducted following similar procedures, here, we only provide a detailed description of assessing the influences of PGQ differences on the differences in retrieved CGC onset timing. To achieve this, for each year between 2006 and 2013, we first divided all the pixels into three groups based on the frequency distribution of the absolute differences in PGQ (dPGQ): from the minimum to the 33th percentile, from the 33th percentile to the 66th percentile, and from the 66th percentile to the maximum. This was to ensure that there were comparable amounts of pixels among the three dPGQ groups, which were hereafter referred to as G1, G2, and G3, respectively. Note that the frequency distribution of dPGQ was determined from PGQ differences from both the first and the second CGC in each year. In other words, we did not distinguish between the first and the second CGC when assessing the PGQ influences. Second, we generated the cumulative distribution function (CDF) of the absolute differences in CGC onset timing in each group. Third, we performed a one-tailed two-sample Kolmogorov–Smirnov test (KS test hereafter) between any two CDFs from the three dPGQ groups (i.e., CDF_{G1} versus CDF_{G2}, CDF_{G2} versus CDF_{G3}, and CDF_{G1} versus CDF_{G3}) using the R package "dgof" [32]. Taking the one-tailed two-sample KS test between the CDFs from G1 and G2 as an example, the null hypothesis was that the CGC onset timing difference in

G1 is greater than or equal to that in G2. By rejecting the null hypothesis, the alternative hypothesis was accepted as that the CGC onset timing difference in G1 is smaller than that in G2 (i.e., the CDF of G1 stays above and to the left of the CDF for G2). The aforementioned three steps were repeated for assessing PGQ influences on the FQI differences and the CGC end timing differences. To investigate the influences of PGQ differences on the differences in the total number of successful CGC retrievals, the three PGQ groups were determined using the mean PGQ difference during 2006–2013 instead of from individual years.

IV. RESULTS

A. Differences Between MODIS and SEVIRI EVI2 Time Series

Fig. 2 shows the differences between the SEVIRI and MODIS EVI2 time series extracted from randomly selected pixels in the three subbasins. The original SEVIRI EVI2 in NCB and SCB presented distinct seasonal cycles, which varied along the reconstructed EVI2 with low uncertainties [see Fig. 2(a) and (c)]. In contrast, the original MODIS EVI2 exhibited more irregular temporal variations, and the good quality observations were sparsely distributed along the reconstructed EVI2. In ECB, the EVI2 observations from both instruments were very irregular [see Fig. 2(b)]. However, the original SEVIRI EVI2 was still able to clearly reflect the double annual cycles of seasonal greenness variations. Nevertheless, the original MODIS EVI2 typically only showed less than five good observations along the reconstructed EVI2 trajectory during a CGC, and the CGCs were poorly portrayed. In some cases, such as during September–December in 2011 and 2012, the CGCs were not able to be retrieved from MODIS EVI2 due to insufficient good quality EVI2 observations.

Fig. 3 presents the spatial patterns of mean PGQ and FQI derived from SEVIRI and MODIS data between 2006 and 2013, respectively, along with the mean and standard deviation of absolute differences in PGQ and FQI. The PGQ derived from SEVIRI data was substantially higher than that derived from MODIS data over much of the Congo Basin [see Fig. 3(a) and (e)]. The SEVIRI PGQ was homogenously high (i.e., above 90%) except for small parts in the southeastern corner and in the east-central Congo Basin [see Fig. 3(a)]. In contrast, the MODIS PGQ was less than 20% at the western and eastern edges of ECB and less than 50% in the central portion of ECB, whereas it was relatively high in both NCB and SCB [see Fig. 3(e)]. The stripes with low PGQ in Fig. 3(e) were caused by gaps between neighboring Terra orbits.

The absolute PGQ difference between SEVIRI and MODIS data increased from less than 30% in northern NCB and southern SCB to between 50% and 80% over much of ECB and at the southwest and northwest corner of NCB and SCB, respectively [see Fig. 3(c)]. The standard deviation of the PGQ difference was less than 20% within the Congo Basin [see Fig. 3(g)]. Despite the significant differences in PGQ, the mean FQI from MODIS data was generally comparable with that inferred from SEVIRI data across the Congo Basin [see Fig. 3(b) and (f)]. Specifically, both the SEVIRI and MODIS FQI varied between 40% and 60% in ECB and between 40% and 100% in NCB
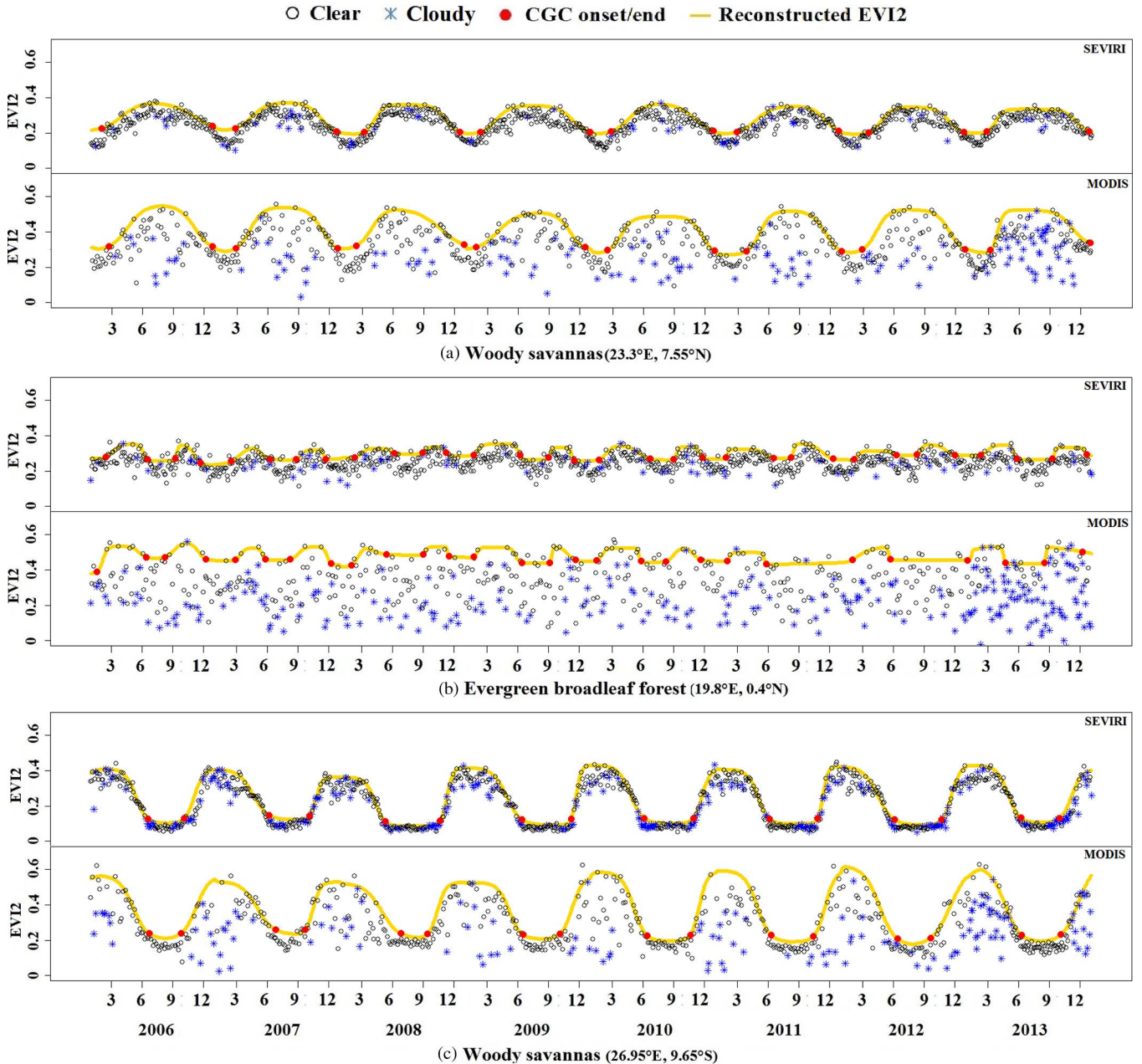
Fig. 2. Original and reconstructed EVI2 temporal trajectories at pixels randomly selected from (a) NCB, (b) ECB, and (c) SCB. Red dots on the ascending and descending phases of a CGC represent the CGC onset and end, respectively. In each MODIS panel, those EVI2s labeled as "clear" correspond to the QA flags of both clear and assumed clear, and those labeled as "cloudy" correspond to the QA flags of "partially cloudy," "cloud shadow," and "cloudy." (a) Woody savannas (23.3° E, 7.55° N). (b) Evergreen broadleaf forest (19.8° E, 0.4° N). (c) Woody savannas (26.95° E, 9.65° S).

and SCB. The absolute FQI difference between SEVIRI and MODIS data and its standard deviation were generally less than 30% and 20% throughout the Congo Basin, respectively [see Fig. 3(d) and (h)].

B. CGCs Derived From SEVIRI and MODIS Data

The statistics for three CGC metrics associated with the EVI2 temporal trajectories presented in Fig. 2 are summarized in Table I. In northern NCB [see Fig. 2(a)], the average length of annual CGC derived from SEVIRI and MODIS data was comparable with a value of 300 and 302 days, respectively. The mean EVI2 amplitude was 0.16 in SEVIRI data and 0.23 in MODIS data, whereas the ratio between EVI2 amplitude

and EVI2 peak (R_{EVI2}) was 0.442 and 0.444 for SEVIRI and MODIS data, respectively. In southern SCB [see Fig. 2(c)], the mean duration of CGC inferred from SEVIRI and MODIS data was 233 and 261 days, respectively. The mean EVI2 amplitude was 0.32 in SEVIRI data and 0.37 in MODIS data, and R_{EVI2} was 0.76 and 0.64, respectively. These results indicate that the CGC duration was longer and the EVI2 amplitude was lower at site a relative to site c. It is likely due to the fact that the plant composites (woody, shrub, and grass species) at these two woody savannas sites are different. Differences in CGC duration and amplitude resulting from changes in plant composites have been identified by previous studies in the African savannas [14], [33]. In ECB [see Fig. 2(b)], the average
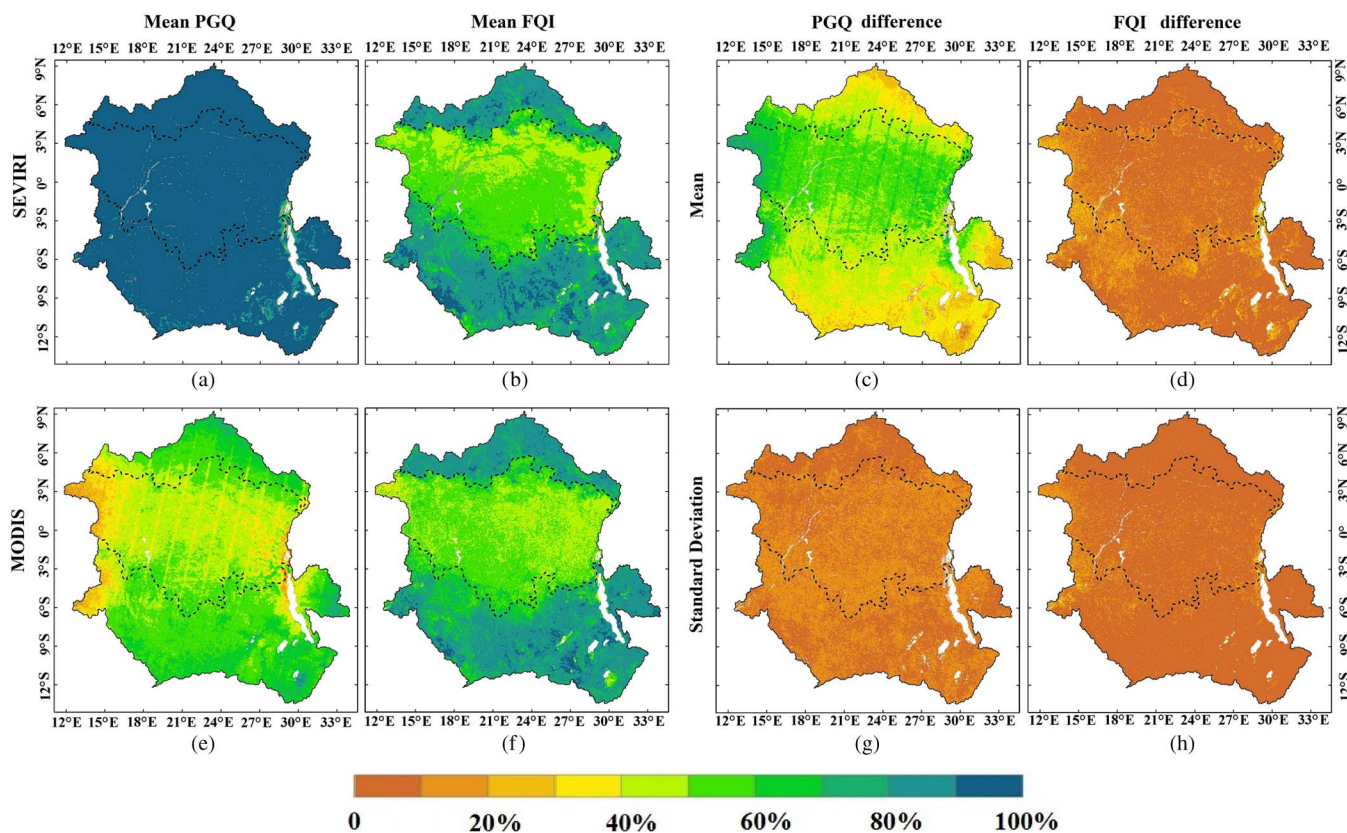
Fig. 3. PGQ and FQI derived from SEVIRI and MODIS data during 2006–2013. (a) Mean SEVIRI PGQ, (b) mean SEVIRI FQI, (c) the mean of absolute difference in PGQ, (d) the mean of absolute difference in FQI, (e) mean MODIS PGQ, (f) mean MODIS FQI, (g) the standard deviation of absolute difference in PGQ, and (h) the standard deviation of absolute difference in FQI. The white color represents water bodies, and the gray color represents the areas without detectable CGC between 2006 and 2013. Black dashed lines represent subbasin boundaries.

TABLE I
SUMMARY OF CGC CHARACTERISTICS AT THE THREE SELECTED PIXELS IN NCB, ECB, AND SCB. SD REPRESENTS STANDARD DEVIATION

Location	Sensor	The first CGC			The second CGC		
		Length (Days)	Amplitude (EVI2 unit)	Amplitude/Peak	Length (Days)	Amplitude (EVI2 unit)	Amplitude/Peak
		Mean (SD)	Mean (SD)	Mean (SD)	Mean (SD)	Mean (SD)	Mean (SD)
NCB (a)	SEVIRI	300.00 (16.00)	0.16 (0.01)	0.442 (0.02)			
	MODIS	302.00 (13.00)	0.23 (0.02)	0.444 (0.02)			
ECB (b)	SEVIRI	125.00 (14.00)	0.09 (0.02)	0.25 (0.05)	90.00 (18.00)	0.09 (0.004)	0.26 (0.02)
	MODIS	118.00 (18.00)	0.11 (0.03)	0.21 (0.06)	100.00 (18.00)	0.09 (0.01)	0.17 (0.02)
SCB (c)	SEVIRI				233.00 (16.00)	0.32 (0.02)	0.76 (0.03)
	MODIS				261.00 (16.00)	0.37 (0.04)	0.64 (0.05)

length of the first CGC was 125 days (SEVIRI) and 118 days (MODIS), whereas the length of the second CGC was 90 days (SEVIRI) and 100 days (MODIS). The mean EVI2 amplitude was subtle, which was 0.09 for both the two CGCs in SEVIRI data and 0.11 and 0.09 for the first and the second cycle in MODIS data, respectively. R_{EVI2} was 0.25 (first CGC) and 0.26 (second CGC) in SEVIRI time series and was 0.21 (first CGC) and 0.17 (second CGC) in MODIS time series, respectively. The standard deviation in CGC length, EVI2 amplitude, and R_{EVI2} varied between 13–18 days, 0.004–0.04 EVI2 units, and 0.02–0.06, respectively.

Fig. 4 shows the spatial shift in mean CGC onset and end timing derived from SEVIRI and MODIS EVI2s. Two annual CGCs existed in ECB. The first CGC initiated around mid-February [see Fig. 4(a) and (e)] and ended in June [see Fig. 4(c) and (g)], whereas the second CGC began between mid-August and mid-September [see Fig. 4(b) and (f)] and

ended in mid- to late November [see Fig. 4(d) and (h)]. Single annual CGC was dominant in NCB and SCB. The mean CGC onset in NCB varied from mid-February in the southern area to as late as mid-April in the northern region [see Fig. 4(a) and (e)], and the CGC end tended to occur during December [see Fig. 4(d) and (h)]. In contrast, the mean CGC onset in SCB varied from early September to mid-November [see Fig. 4(b) and (f)], and the end of CGC occurred between mid-June and mid-July of the next year [see Fig. 4(c) and (g)].

The variations in the latitudinal averages of the mean CGC onset and end timings present the overall shift patterns of the two annual CGCs in the Congo Basin (see Fig. 5). The latitudinal averages of both CGC onset and end timings exhibited fluctuations across the subbasins. The CGC onset and end in the first cycle occurred during late February to early March and during mid- to late December, respectively, within 8° N-6° S. The CGC onset and end in the second cycle
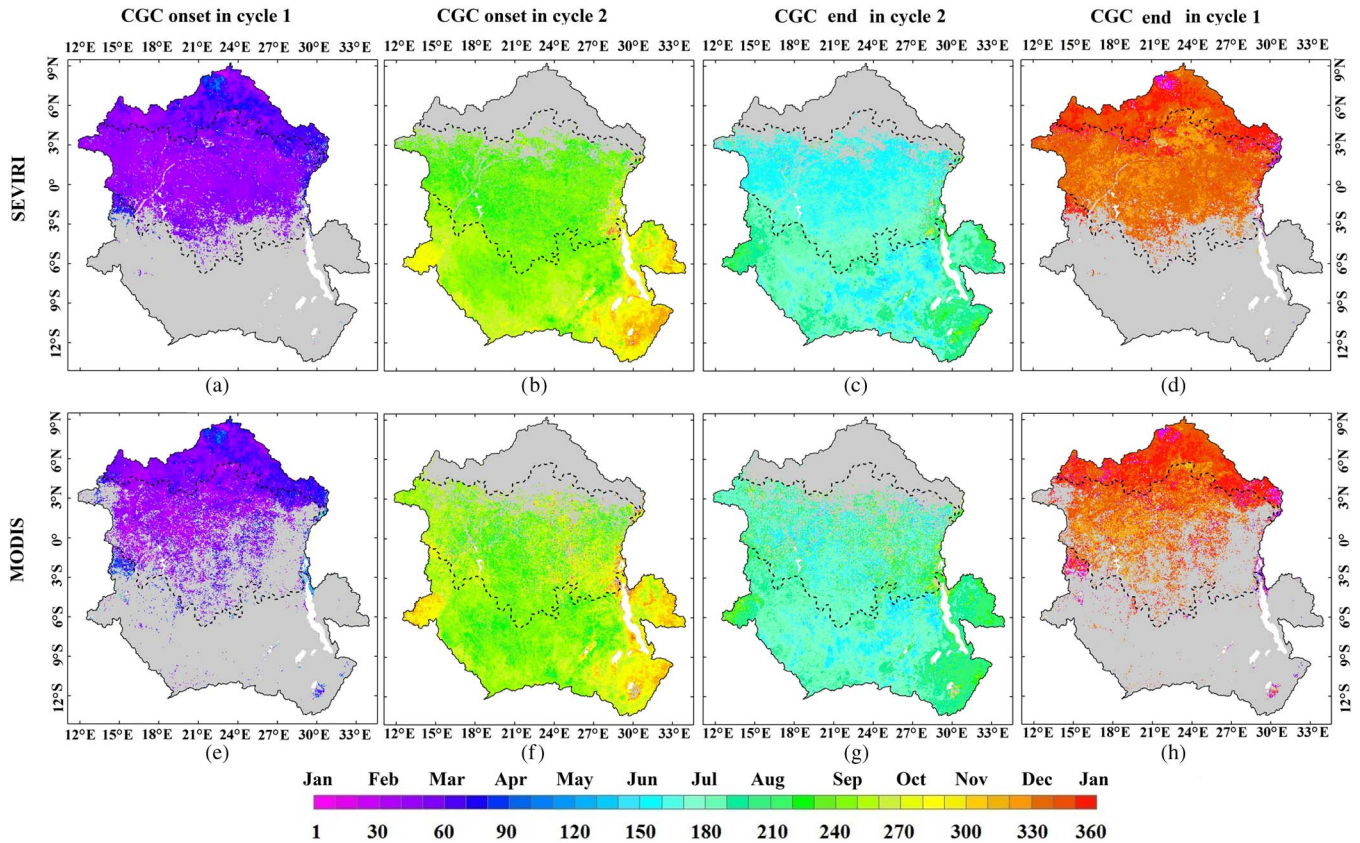
Fig. 4. Mean onset and end of CGC derived from SEVIRI and MODIS data between 2006 and 2013 across the Congo Basin. The CGC onset in the first cycle from (a) SEVIRI and (e) MODIS, CGC onset in the second cycle from (b) SEVIRI and (f) MODIS, CGC end in the second cycle from (c) SEVIRI and (g) MODIS, and CGC end in the first cycle from (d) SEVIRI and (h) MODIS. Note that the onset and end of the first CGC in ECB occurs in the first and second cycles, respectively. The onset and end of the second CGC in ECB occurs in the second and first cycles, respectively. The gray area indicates that the specified CGC transition event was detected less than four times between 2006 and 2013. Others are the same as the illustration in Fig. 3.
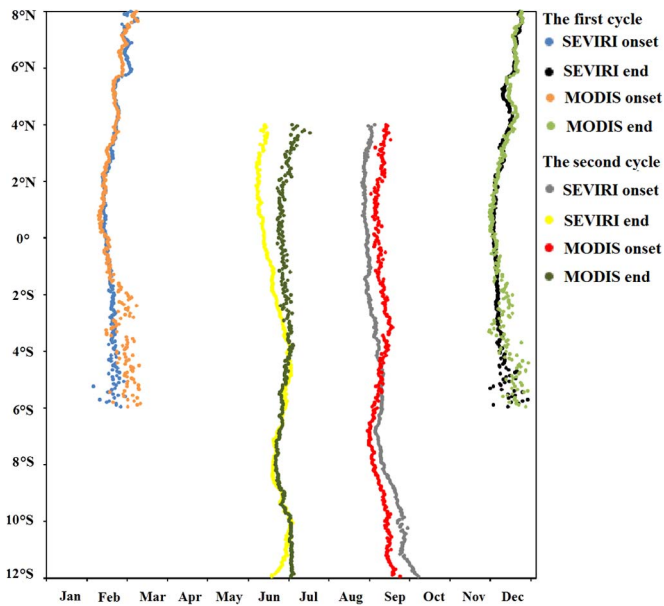

Fig. 5. Spatial variations in the latitudinal averages of SEVIRI- and MODIS-derived mean CGC onset and end timings across the Congo Basin. Note that the two annual CGCs in ECB should be interpreted the same way as that in Fig. 4.

unfolded between mid-September and mid-October and between mid-June and mid-July in the next year, respectively, within 4° N–12° S. The maximum of the absolute difference between SEVIRI- and MODIS-derived latitudinal averages in-

creased from about 18 days for the CGC onset in the second cycle to as high as 32 days for the CGC end in the second cycle.

The most evident inconsistency between the distributions of CGC detected from SEVIRI and MODIS EVI2s was found in ECB. Specifically, double annual CGCs derived from SEVIRI EVI2 existed over much of ECB [see Fig. 4(a)–(d)]. In contrast, double annual CGCs derived from MODIS EVI2 distributed predominately in the central and western ECB [see Fig. 4(e)–(h)]. In ECB, the detection rate of double annual CGCs by MODIS was about 34% lower than that from SEVIRI (a mean value of 73.7% and 39.4% for SEVIRI and MODIS, respectively) (see Fig. 6). This is due to the limited cloud-free observations in the MODIS time series [e.g., the CGC detection failures during September–December in 2011 and 2012 at the evergreen broadleaf forest location in Fig. 2(b)]. Relatively, the difference in CGC detection rate between MODIS and SEVIRI greatly reduced in NCB and SCB (see Fig. 6), where CGC was detected at more than 95% of the pixels from SEVIRI and over 88% from MODIS. The standard deviation in CGC detection rate increased from NCB (0.91% for SEVIRI and 1.85% for MODIS) and SCB (1.51% for SEVIRI and 1.82% for MODIS) toward ECB (6.07% for SEVIRI and 3.88% for MODIS) (see Fig. 6).

Fig. 7 displays the mean and standard deviation in the absolute timing differences between SEVIRI- and MODIS-derived CGC onset and end timings during 2006–2013. In
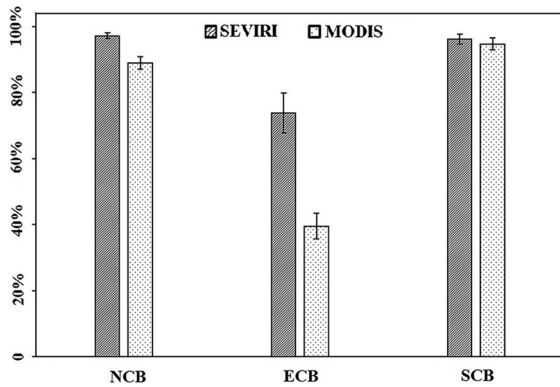
Fig. 6. Mean and standard deviation in CGC detection rate using SEVIRI and MODIS EVI2s between 2006 and 2013 across the three subbasins. Gray and white bars represent the SEVIRI- and MODIS-derived mean detection rates, respectively. The error bars indicate one standard deviation from the mean.

NCB, the timing differences were mostly less than 20 days for both CGC onset [see Fig. 7(a)] and CGC end [see Fig. 7(d)], and the difference of 20–40 days was more widespread for CGC onset than for CGC end. In SCB, the timing difference was predominately less than 20 days for both CGC onset [see Fig. 7(b)] and CGC end [see Fig. 7(c)]. However, the timing difference of more than 20 days was also found in small areas scattering over western, southeastern, and eastern SCB, which might have resulted from local environmental factors that could have significant impacts on CGC detections, such as the air pollution [34] and adjacent water body in the Kinshasa City (4.4° S, 15.3° E) of the Democratic Republic of the Congo. The timing difference was mostly between 20 and 40 days in ECB [see Fig. 7(a)–(d)]. The standard deviations of timing differences in CGC onset and end were generally less than 20 days in NCB and SCB [see Fig. 7(e)–(h)]. The standard deviations of less than 20 days mixed with those between 20 and 40 days in ECB [see Fig. 7(e)–(h)].

Fig. 8 shows the absolute differences in the total number of successful CGC retrievals from SEVIRI and MODIS EVI2 time series during 2006–2013. The differences in both NCB and SCB were generally less than two, which indicated the comparable performances in CGC retrievals from SEVIRI and MODIS. A major exception was found at the Bangweulu swamps (11.5° S, 30.1° E) in southwestern SCB where the difference was up to seven due to the likely false CGC onsets retrieved from MODIS data as a result of prolonged cloud contaminations. However, substantial differences were observed in ECB. For the first CGC [see Fig. 8(a)], the difference mainly varied between two and six and could be larger than six in the eastern and northwestern ECB. The difference in the second CGC was much smaller than that for the first CGC [see Fig. 8(b)]. The areas with a difference of more than two were sparsely distributed across ECB.

C. Impacts of Quality of EVI2 Time Series on CGC Detections

Table II summarizes the range of dPGQ and the number of 0.05° pixels in G1, G2, and G3. Since the number of pixels was set to be comparable among the three groups, the dPGQ range in each group varied between years. Between 2006 and

2013, dPGQ was in the range of 0%–46%, 26%–60%, and 37%–98% for G1, G2, and G3, respectively. The last row of Table II provides the range of mean dPGQ and the number of pixels in G1, G2, and G3, based on which we assessed the influences of PGQ differences on the differences in the total number of successful CGC retrievals.

Fig. 9 presents the comparisons of CDFs in the FQI differences among the three dPGQ groups. Across the eight years between 2006 and 2013, the absolute difference in FQI was less than 10% in 50% of the pixels and less than 34% in 95% of the pixels in all the three dPGQ groups. The KS tests showed that, throughout the years between 2006 and 2013, the CDFs of FQI differences were significantly different ($p < 0.001$) among the three dPGQ groups, and the FQI differences in the groups with small PGQ differences were all significantly less than those from the groups with large PGQ differences. The only exception was found in the comparison between the CDFs of G1 and G2 and between G1 and G3 in 2007 [see Fig. 9(b). While the CDF for G1 was significantly larger than that for G2 ($p < 0.001$), no significant difference was found between the CDFs for G1 and G3 in 2007.

Figs. 10 and 11 present the comparisons of CDFs in the absolute timing differences in CGC onset and end among the three dPGQ groups, respectively. The median of CGC onset differences was less than 19 days and less than 16 days for CGC end differences in all the three groups. The 95th percentile of CGC onset differences fell in the range of 41–52 days, 42–53 days, and 42–61 days during 2006–2013 for G1, G2, and G3, respectively. Similarly, the 95th percentile of CGC end differences was in the range of 35–46 days, 36–46 days, and 40–52 days during 2006–2013 for G1, G2, and G3, respectively. Those results indicated that the differences in PGQ had significant influences on the timing differences in CGC onset and end. KS tests were significant in all eight years ($P < 0.0001$) when comparing the CDFs of onset or end timing differences in G1 versus those in G3 or those in G2 versus those in G3. Those comparisons revealed that larger timing differences in CGC onset or end were associated with larger PGQ differences. Similar results were also found when comparing the CDFs of onset or end timing differences in G1 versus those in G2 in most years, but there were some exceptions. Specifically, the timing difference in G1 was found to be larger than that in G2 in 2006, 2007, and 2010 for the CGC onset [see Fig. 10(a), (b), and (e)] and in 2007 for the CGC end [see Fig. 11(b)]. The case of no significant difference between the CGC onset timing in G1 and G2 was identified in 2013 [see Fig. 10(h)] and in 2010 for the CGC end timing [see Fig. 11(e)].

Fig. 12 displays the comparison of CDFs for the absolute differences in the total number of successful CGC retrievals among the three dPGQ groups. The median of the difference in total successful CGC retrievals was less than two in all the three groups, whereas the 95th percentile was two, four, and five for G1, G2, and G3, respectively. Results from KS tests indicated that the PGQ difference had significant influences on the differences in the total number of successful CGC retrievals and large dPGQ resulted in large difference in successful CGC retrievals.
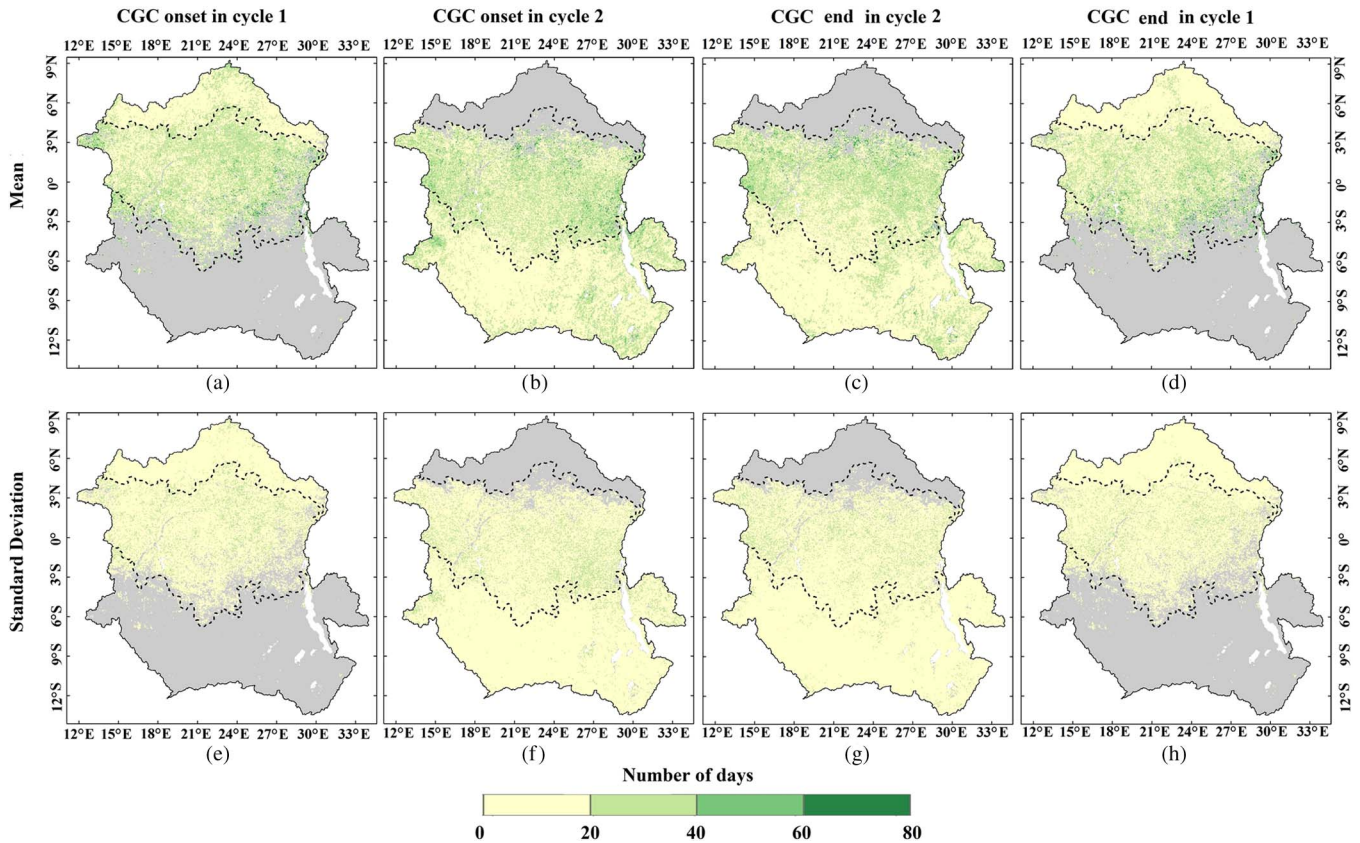
Fig. 7.   Mean and standard deviation in the absolute differences between SEVIRI- and MODIS-derived CGC onset and end timings during 2006–2013. The mean value of timing differences in (a) CGC onset in the first cycle, (b) CGC onset in the second cycle, (c) CGC end in the second cycle, and (d) CGC end in the first cycle. The standard deviation of timing differences in (e) CGC onset in the first cycle, (f) CGC onset in the second cycle, (g) CGC end in the second cycle, and (h) CGC end in the first cycle. Note that the two annual CGCs in ECB should be interpreted the same way as that in Fig. 4. The gray area indicates that the specified CGC transition event was not detected during 2006–2013. Others are the same as the illustration in Fig. 3.
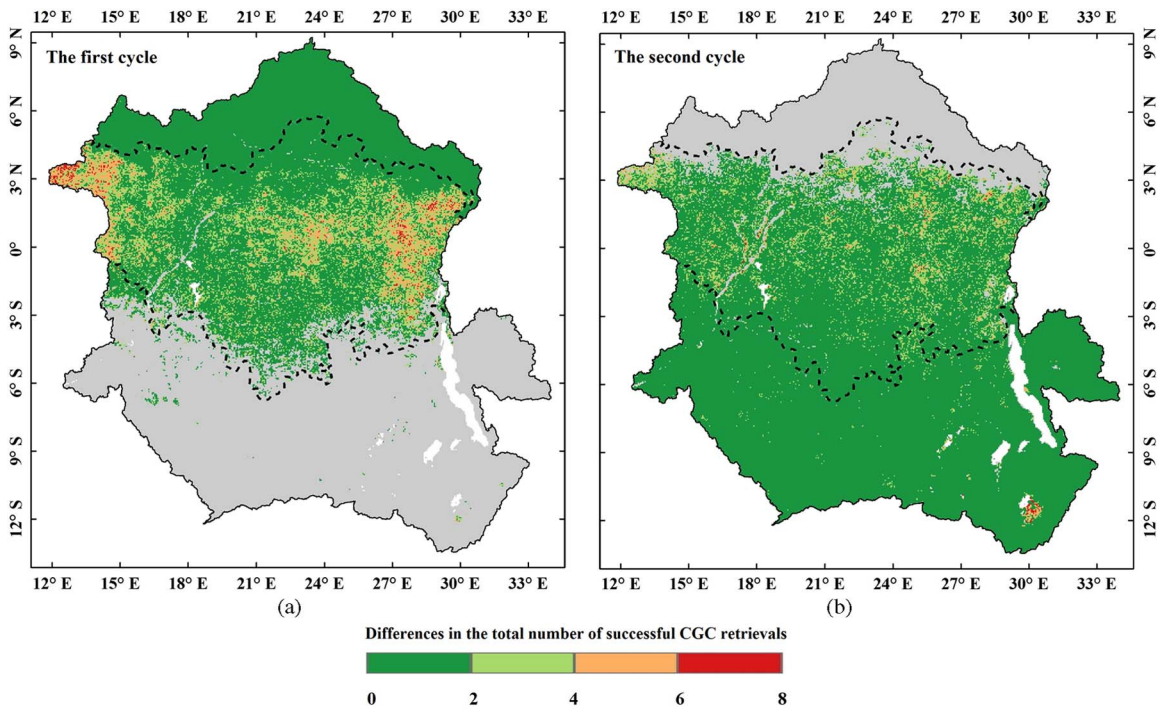

Fig. 8.   Absolute difference in the total number of successful CGC retrievals in the (a) first and the (b) second cycle from SEVIRI and MODIS during 2006–2013. The gray area indicates that the CGC in the specified cycle was not detected during 2006–2013. Others are the same as the illustration in Fig. 3.

TABLE II
SUMMARY OF THE RANGE OF PGQ DIFFERENCE AND THE NUMBER OF PIXELS IN EACH GROUP. dPGQ REPRESENTS
THE ABSOLUTE DIFFERENCE IN PGQ, AND NOP IS THE NUMBER OF $0.05°$ PIXELS

|	G1		G2		G3	
	Range	NOP	Range	NOP	Range	NOP
2006	$0 <= dPGQ < 42\%$	34051	$42\% <= dPGQ < 53\%$	38139	$53\% <= dPGQ <= 98\%$	40800
2007	$0 <= dPGQ < 34\%$	35840	$34\% <= dPGQ < 47\%$	33835	$47\% <= dPGQ <= 96\%$	39292
2008	$0 <= dPGQ < 43\%$	34400	$43\% <= dPGQ < 55\%$	38328	$55\% <= dPGQ <= 97\%$	39882
2009	$0 <= dPGQ < 43\%$	36482	$43\% <= dPGQ < 54\%$	36401	$54\% <= dPGQ <= 98\%$	40260
2010	$0 <= dPGQ < 40\%$	34959	$40\% <= dPGQ < 51\%$	35446	$51\% <= dPGQ <= 97\%$	38447
2011	$0 <= dPGQ < 46\%$	34741	$46\% <= dPGQ < 57\%$	34711	$57\% <= dPGQ <= 95\%$	37540
2012	$0 <= dPGQ < 46\%$	33778	$46\% <= dPGQ < 60\%$	37290	$60\% <= dPGQ <= 97\%$	36837
2013	$0 <= dPGQ < 26\%$	35580	$26\% <= dPGQ < 37\%$	35838	$37\% <= dPGQ <= 95\%$	38937
Mean	$0 <= dPGQ < 45\%$	39717	$45\% <= dPGQ < 55\%$	39723	$55\% <= dPGQ <= 97\%$	40920
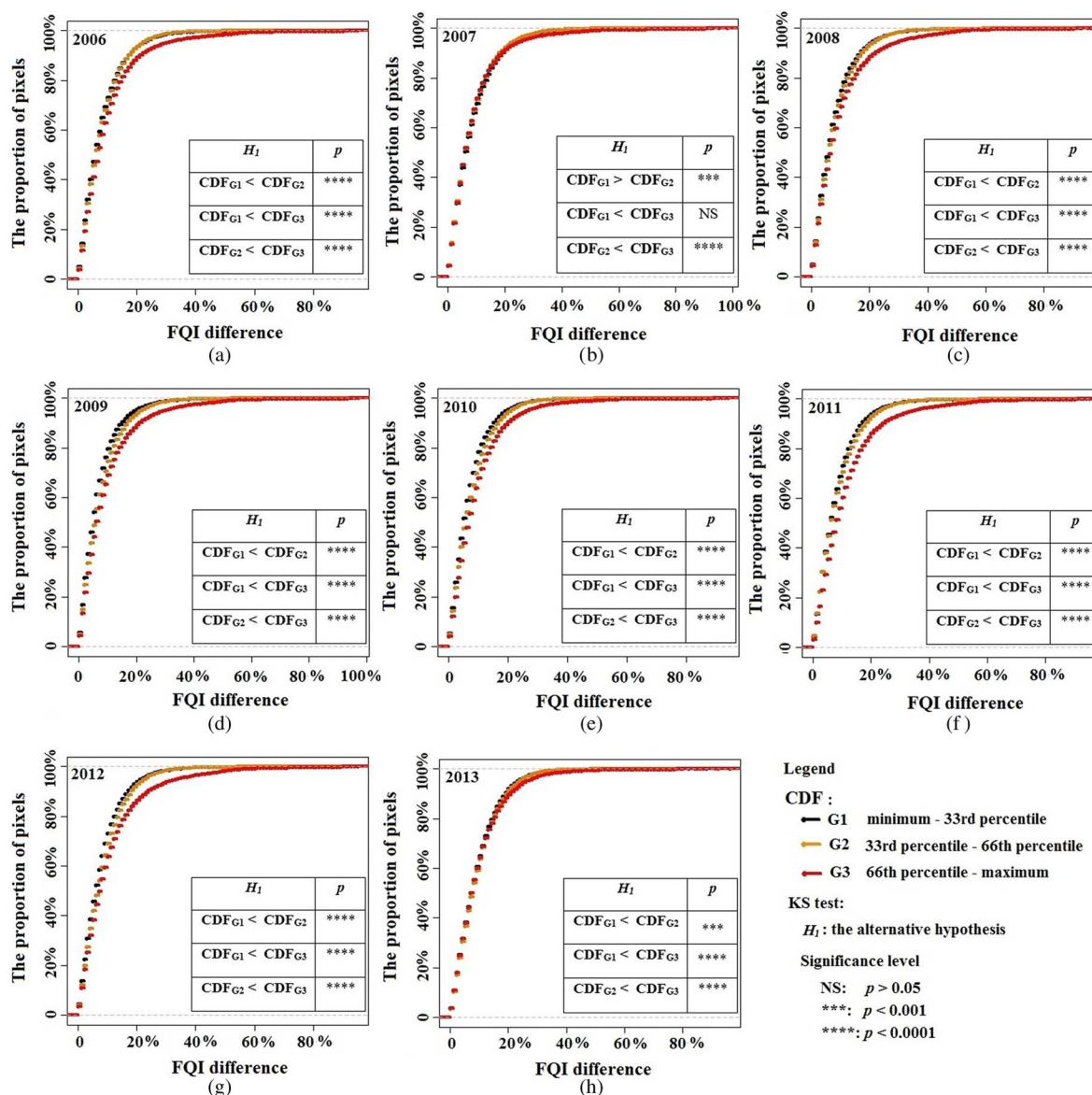
Fig. 9. Comparison of CDFs for the absolute FQI differences in the three dPGQ groups and the results of KS tests. The x-axis shows the absolute FQI differences, and the y-axis shows the proportion of pixels. Black, orange, and red step curves represent the CDF for G1, G2, and G3, respectively. The table in the lower right corner of each panel presents the three alternative hypotheses and the corresponding significance levels.

V. DISCUSSION

This paper demonstrated that EVI2 time series from SEVIRI and MODIS had comparable performances in detecting the single annual CGC in the woody-savanna-dominated NCB and SCB, whereas SEVIRI EVI2 time series outperformed that from MODIS by detecting the double annual CGCs within a more widespread region in the rainforest-dominated ECB.
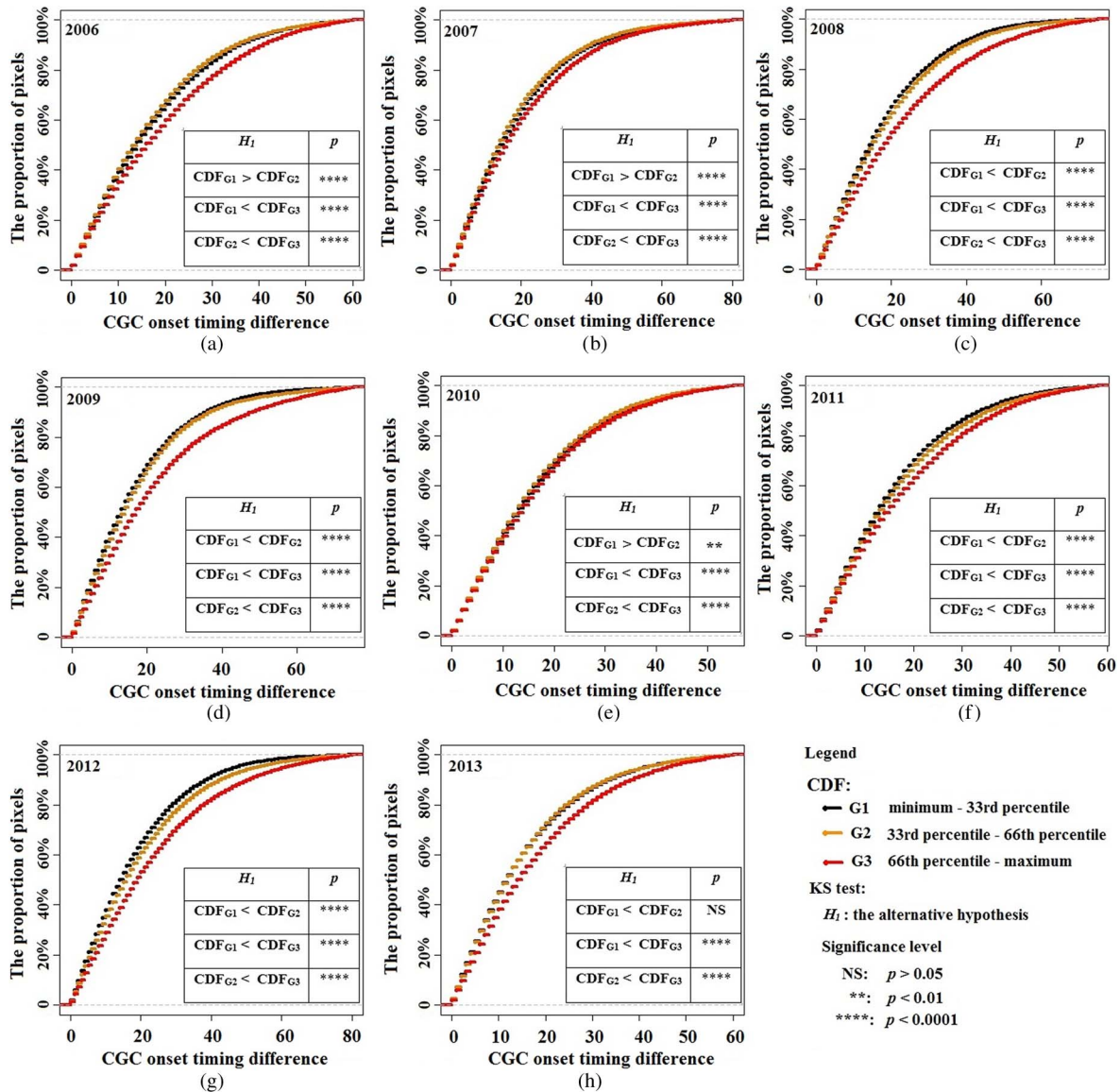
Fig. 10. Comparison of CDFs for the absolute timing differences in detected CGC onset in the three dPGQ groups and the result of KS tests. The x-axis shows the absolute timing differences in detected CGC onset (number of days), and the y-axis shows the proportion of pixels. Others are the same as the illustration in Fig. 9.

Specifically, the CGC detection rate from SEVIRI was about 34% higher than that from MODIS in ECB. The better performance of SEVIRI EVI2 in ECB can be attributed to the frequent diurnal scanning by SEVIRI, which provided much higher chances to obtain cloud-free observations than MODIS did. The superior performance of SEVIRI over MODIS in terms of obtaining cloud-free observations was also reported by a study in the cloud-prone West Africa [15]. Despite the differences in the distribution of detected double annual CGCs in ECB, the overall patterns of the spatial shifts in CGC onset and end timings derived from both SEVIRI and MODIS agreed with those identified in a previous study [17].

The difference in PGQ between MODIS and SEVIRI EVI2 time series was the main source of the inconsistencies in the detected CGC onset and end timings. Specifically, SEVIRI PGQ was homogeneously high over much of the Congo Basin, whereas MODIS PGQ exhibited decreases from NCB and SCB to ECB. PGQ differences between MODIS and SEVIRI EVI2

time series increased from less than 30% in NCB and SCB to as high as 80% in ECB. As a result, the differences in the detected timing of either CGC onset or end increased from mostly less than 20 days in NCB and SCB to predominately between 20 and 60 days in ECB, and the difference of more than 60 days was also observed at some isolated locations within ECB. The timing difference identified in this paper is comparable with the result from a previous study, in which maximum timing differences of 43 (for CGC onset) and 65 days (for CGC end) during 2008–2009 between MODIS and SEVIRI detections are reported [18]. Results from the KS tests between the three dPGQ groups indicated that large timing differences in CGC onset and end were significantly associated with large PGQ differences in most years. However, we did identify a few cases where relatively large timing differences were found in groups with relatively small PGQ difference [see, e.g., Figs. 10(a), (b), and (e) and 11(b)] or no significant timing difference between two dPGQ groups was identified [see, e.g.,
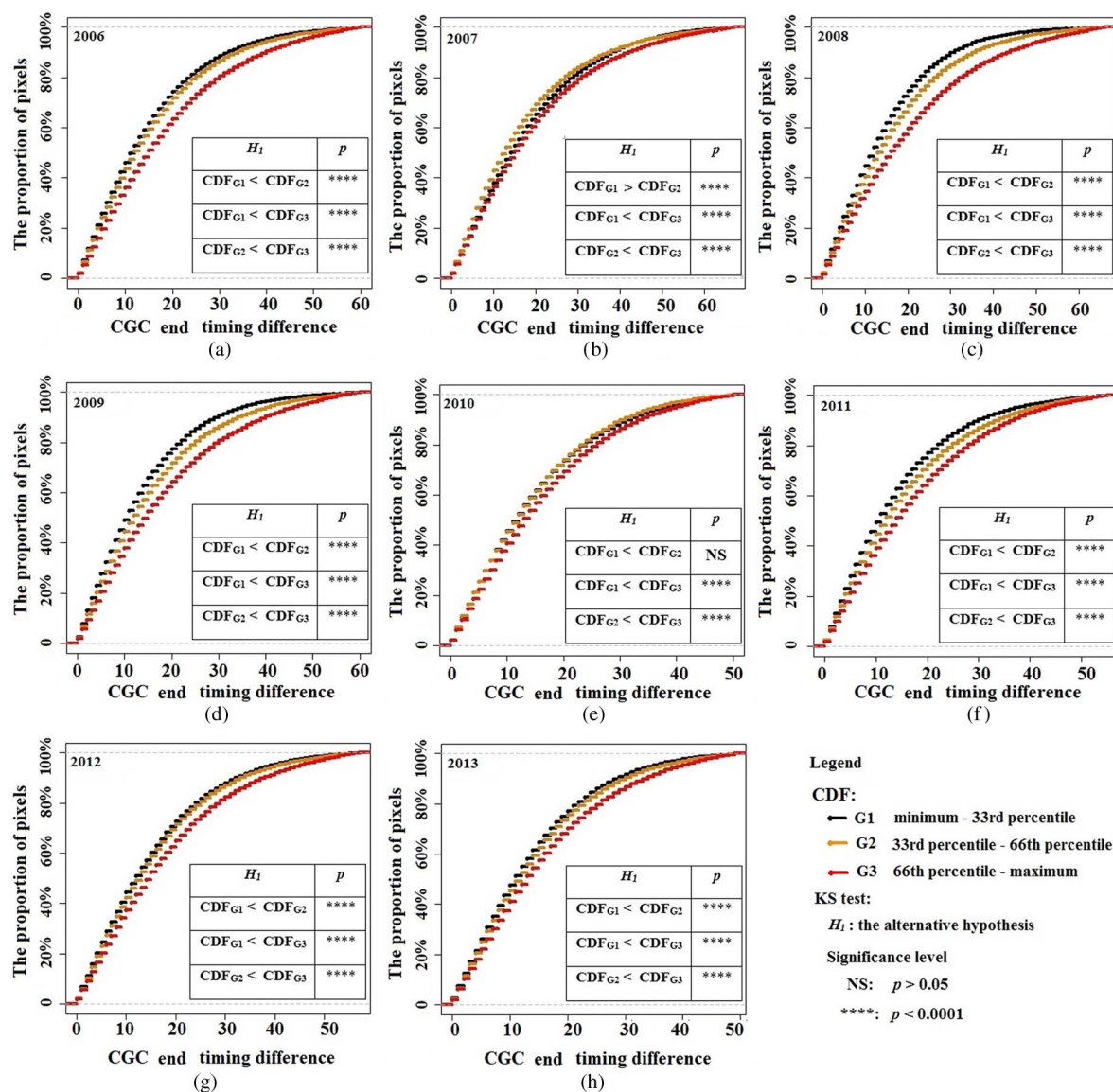
Fig. 11. Comparison of CDFs for the absolute timing differences in detected CGC end in the three dPGQ groups and the result of KS tests. The x-axis shows the absolute timing differences in detected CGC end (number of days), and the y-axis shows the proportion of pixels. Others are the same as the illustration in Fig. 9.

Figs. 10(h) and 11(e)]. This can be explained by the fact that, since PGQ provides an overall measurement of EVI2 quality during a CGC, the difference in PGQ might not be able to account for the difference in the retrieved timing of an individual CGC transition event (e.g., CGC onset or end) in every case. We believe that the differences in local PGQ around the timing of an individual CGC transition event should be explored in those cases.

The FQIs of the reconstructed SEVIRI and MODIS EVI2 trajectories both exhibited decreases from NCB and SCB to ECB. SEVIRI FQI was low in ECB relative to the high SEVIRI PGQ. This was likely due to the fact that good quality observations identified in SEVIRI data within ECB were contaminated by partial clouds or by cirrus clouds. The method that we used for cloud screening only classifies a pixel into cloud-free or cloudy without applying a buffer mask to account for the residual contaminations resulting from cloud edges. In addition, it is difficult to identify cirrus cloud contamination since SEVIRI

is not equipped with the channel for cirrus cloud detection (i.e., 1.36–1.38 μm) [35]. Given the relatively large pixel size ($\sim$3–5 km) used in this paper, some pixels with a QA flag of "cloud-free" were likely affected by residual cloud contaminations, which were evident in the SEVIRI EVI2 trajectories shown in Fig. 2(b). Specifically, some suspiciously low EVI2 values during a CGC were assigned the QA flag of "cloud-free," which have negative influences on SEVIRI FQI by increasing the differences between the original EVI2 with good quality and the corresponding reconstructed EVI2. However, a high FQI value does not necessarily indicate that the EVI2 temporal trajectory is reasonably reconstructed if the PGQ is limited (e.g., the high MODIS FQI in ECB relative to the low MODIS PGQ). For example, if there are three good quality values in a time series of ten observations, the good quality values could be perfectly fitted by various functions. However, the fitted curve may not be able to represent the other seven values reasonably. Therefore, a reliable CGC detection is possible only
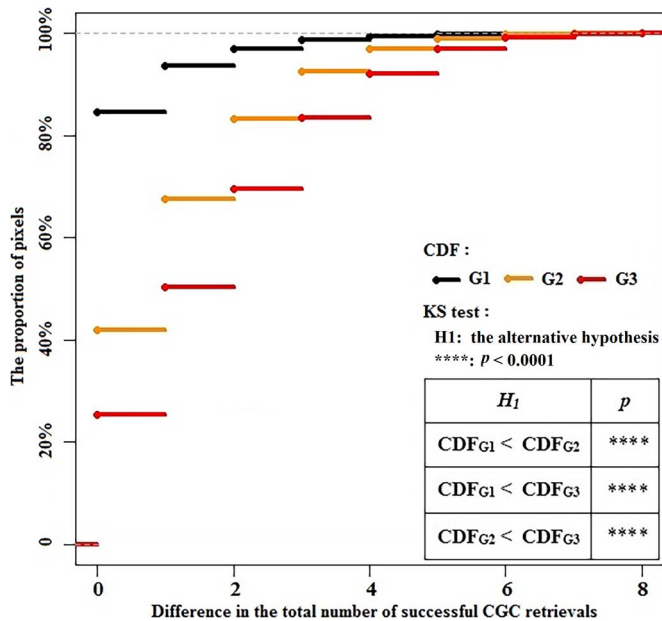
Fig. 12. Comparison of CDFs for the absolute differences in the total number of successful CGC retrievals in the three dPGQ groups and the result of KS tests. The x-axis shows the absolute differences in the total number of successful CGC retrievals, and the y-axis shows the proportion of pixels. Others are the same as the illustration in Fig. 9.

with high PGQ. PGQ differences only had limited influences on FQI differences. Specifically, the CDFs for FQI differences in the three dPGQ groups closely resembled each other, and the absolute difference in FQI was less than 10% in 50% of the pixels and less than 34% in 95% of the pixels in all the three dPGQ groups across the eight years. This also indicates that the HPLM is robust in the reconstruction of EVI2 temporal trajectories from good quality observations. In other words, observations with good quality in the EVI2 time series are well represented in the reconstructed trajectories. Note that, if there are locations where the duration of a dormancy period is less than a month, the EVI2 variation (i.e., quick transition from decreasing EVI2 to increasing EVI2) during the dormancy period could be poorly portrayed in the reconstructed EVI2 trajectory. As a result, the retrieved timings of CGC onset and end would be biased at those locations.

The most evident influence of PGQ difference on LSP retrievals was revealed by the differences in the total number of successful CGC retrievals. Unlike the CDFs of the differences in FQI and CGC timing, the CDFs of the differences in the total number of successful CGC retrievals for the three dPGQ groups differed dramatically from each other. This could be explained by the fact that PGQ was an indicator of the overall EVI2 quality during a CGC and accounted well for the overall differences in CGC detections from MODIS and SEVIRI time series.

VI. Conclusion

This paper compared the CGC retrieved from SEVIRI and MODIS EVI2 time series across the Congo Basin between 2006 and 2013. While SEVIRI and MODIS had comparable performances in detecting the single annual CGC within the woody-savanna-dominated NCB and SCB, SEVIRI outperformed MODIS by detecting the double annual CGCs within

a more widespread region in the tropical-rainforest-dominated ECB. The advantage of SEVIRI over MODIS in CGC retrievals within ECB can be attributed to the frequent diurnal observations by SEVIRI, which provided higher chances to obtain cloud-free observations. Differences in PGQ had significant influences on the timing differences in the retrieved CGC onset and end, and the total number of successful CGC retrievals. This suggests that using the time series of satellite data with limited good quality observations would result in large uncertainties in the retrievals of phenological timing and even cause failures in phenological cycle retrievals. This indicates that satellite data quality would have significant impacts on the understanding of ecosystem properties. Therefore, changes inferred from satellite observations in cloud-prone regions should be carefully interpreted.

The monitoring of global tropical rainforest phenology using a set of geostationary satellites is very promising. Specifically, the next generation of geostationary satellites such as the Himawari-8 has been launched in October 2014 (http://www.data.jma.go.jp/mscweb/en/operation8/index.html), which covers the Asia-Pacific region. The first launch of the Geostationary Operational Environmental Satellite-R Series (GOES-R) is scheduled in late 2016 (http://www.goes-r.gov/mission/mission.html), which covers North America and South America. Sensors on those satellites provide visible and near-infrared observations at a spatial resolution of 0.5–1.0 km. The observations from those geostationary satellites would enhance the knowledge of long-term changes in rainforest phenology in other major rainforest ecosystems such as the Amazon Basin and the Asia monsoon region.

References

[1] Y. Malhi *et al.*, "African rainforests: Past, present and future," *Phil. Trans. R. Soc. B, Biol. Sci.*, vol. 368, no. 1625, Sep. 2013, Art. no. 20120312.

[2] S. L. Lewis *et al.*, "Increasing carbon storage in intact African tropical forests," *Nature*, vol. 457, no. 7232, pp. 1003–1006, Feb. 2009.

[3] C. Megevand *et al.*, *Deforestation Trends in the Congo Basin: Reconciling Economic Growth and Forest Protection*. Washington, DC, USA: World Bank, 2013, pp. 29–42.

[4] P. V. Potapov *et al.*, "Quantifying forest cover loss in Democratic Republic of the Congo, 2000–2010, with Landsat ETM + data," *Remote Sens. Environ.*, vol. 122, pp. 106–116, Jul. 2012.

[5] M. de Weirdt *et al.*, "Seasonal leaf dynamics for tropical evergreen forests in a process-based global ecosystem model," *Geosci. Model Develop.*, vol. 5, no. 5, pp. 1091–1108, Sep. 2012.

[6] C. Couralet *et al.*, "Phenology in functional groups of central African rainforest trees," *J. Tropical Forest Sci.*, vol. 25, no. 3, pp. 361–374, Jul. 2013.

[7] G. Viennois *et al.*, "Multiresolution quantification of deciduousness in West-Central African forests," *Biogeosciences*, vol. 10, no. 11, pp. 6957–6967, Nov. 2013.

[8] B. Poulter, U. Heyder, and W. Cramer, "Modeling the sensitivity of the seasonal cycle of GPP to dynamic LAI and soil depths in tropical rainforests," *Ecosystems*, vol. 12, no. 4, pp. 517–533, Jun. 2009.

[9] K. M. de Beurs and G. M. Henebry, "Land surface phenology and temperature variation in the International Geosphere-Biosphere Program high-latitude transects," *Global Change Biol.*, vol. 11, no. 5, pp. 779–790, 2005.

[10] X. Zhang *et al.*, "Monitoring vegetation phenology using MODIS," *Remote Sens. Environ.*, vol. 84, no. 3, pp. 471–475, Nov. 2003.

[11] F. Maignan *et al.*, "Interannual vegetation phenology estimates from global AVHRR measurements: Comparison with *in situ* data and applications," *Remote Sens. Environ.*, vol. 112, no. 2, pp. 496–505, Feb. 2008.

[12] X. Zhang, M. A. Friedl, and C. B. Schaaf, "Global vegetation phenology from Moderate Resolution Imaging Spectroradiometer (MODIS): Evaluation of global patterns and comparison with *in situ* measurements," *J. Geophys. Res., Biogeosci.*, vol. 111, no. G4, Dec. 2006, Art. no. G04017.

[13] V. Gond *et al.*, "Vegetation structure and greenness in Central Africa from MODIS multi-temporal data," *Phil. Trans. R. Soc. B, Biol. Sci.*, vol. 368, no. 1625, Sep. 2013, Art. no. 20120309.

[14] A. Verhegghen *et al.*, "Mapping Congo Basin vegetation types from 300 m and 1 km multi-sensor time series for carbon stocks and forest areas estimation," *Biogeosciences*, vol. 9, no. 12, pp. 5061–5079, Dec. 2012.

[15] R. Fensholt *et al.*, "Comparisons of compositing period length for vegetation index data from polar-orbiting and geostationary satellites for the cloud-prone region of West Africa," *Photogram. Eng. Remote Sens.*, vol. 73, no. 3, pp. 297–309, Mar. 2007.

[16] X. Zhang, M. A. Friedl, and C. B. Schaaf, "Sensitivity of vegetation phenology detection to the temporal resolution of satellite data," *Int. J. Remote Sens.*, vol. 30, no. 8, pp. 2061–2074, Apr. 2009.

[17] K. Guan *et al.*, "Deriving vegetation phenological time and trajectory information over Africa using SEVIRI daily LAI," *IEEE Trans. Geosci. Remote Sens.*, vol. 52, no. 2, pp. 1113–1130, Feb. 2014.

[18] J. S. Sobrino, Y. Julien, and G. Soria, "Phenology estimation from Meteosat second generation data," *IEEE J. Sel. Topics Appl. Earth Observ. Remote Sens.*, vol. 6, no. 3, pp. 1653–1659, Jun. 2013.

[19] M. A. Friedl *et al.*, "MODIS Collection 5 global land cover: Algorithm refinements and characterization of new datasets," *Remote Sens. Environ.*, vol. 114, no. 1, pp. 168–182, Oct. 2010.

[20] M. A. White, P. E. Thornton, and S. W. Running, "A continental phenology model for monitoring vegetation responses to interannual climatic variability," *Global Biogeochem. Cycles*, vol. 11, no. 2, pp. 217–234, Sep. 1997.

[21] B. C. Reed *et al.*, "Measuring phenological variability from satellite imagery," *J. Vegetation Sci.*, vol. 5, no. 5, pp. 703–714, Nov. 1994.

[22] R. Fensholt *et al.*, "Analysing NDVI for the African continent using the geostationary Meteosat second generation SEVIRI sensor," *Remote Sens. Environ.*, vol. 101, no. 2, pp. 212–229, Feb. 2006.

[23] "Conversion from radiances to reflectances for SEVIRI warm channels," EUMETSAT, Darmstadt, Germany, Rep. no. EUM/MET/TEN/12/0332, 2012. [Online]. Available: http://www.eumetsat.int/website/home/Data/Products/Calibration/MSGCalibration/index.html

[24] C. J. Merchant *et al.*, "Probabilistic physically based cloud screening of satellite infrared imagery for operational sea surface temperature retrieval," *Q. J. R. Meteorol. Soc.*, vol. 131, no. 611, pp. 2735–2755, Dec. 2005.

[25] Z. Jiang *et al.*, "Development of a two-band enhanced vegetation index without a blue band," *Remote Sens. Environ.*, vol. 112, no. 10, pp. 3833–3845, Mar. 2008.

[26] A. Huete *et al.*, "Overview of the radiometric and biophysical performance of the MODIS vegetation indices," *Remote Sens. Environ.*, vol. 83, no. 1/2, pp. 195–213, Nov. 2002.

[27] A. V. Rocha and G. R. Shaver, "Advantages of a two band EVI calculated from solar and photosynthetically active radiation fluxes," *Agricul. Forest Meteorol.*, vol. 149, no. 9, pp. 1560–1563, Sep. 2009.

[28] Y. Tian *et al.*, "Analysis of vegetation index NDVI anisotropy to improve the accuracy of the GOES-R green vegetation fraction product," in *Proc. IEEE IGARSS*, 2010, pp. 2091–2094.

[29] E. Vermote, C. O. Justice, and F. M. Breon, "Towards a generalized approach for correction of the BRDF effect in MODIS directional reflectances," *IEEE Trans. Geosci. Remote Sens.*, vol. 47, no. 3, pp. 898–908, Mar. 2009.

[30] X. Zhang, "Reconstruction of a complete global time series of daily vegetation index trajectory from long-term AVHRR data," *Remote Sens. Environ.*, vol. 156, pp. 457–472, Nov. 2015.

[31] X. Zhang *et al.*, "Monitoring the response of vegetation phenology to precipitation in Africa by coupling MODIS and TRMM instruments," *J. Geophys. Res., Atmosp.*, vol. 110, no. D12, Jun. 2005, Art. no. D12103.

[32] T. B. Arnold and J. W. Emerson, "Nonparametric goodness-of-fit tests for discrete null distributions," *R Journal*, vol. 3/2, pp. 34–39, Dec. 2011.

[33] C. M. Ryan *et al.*, "Assessing the phenology of southern tropical Africa: A comparison of hemispherical photography, scatterometry, and optical/NIR remote sensing," *IEEE Trans. Geosci. Remote Sens.*, vol. 52, no. 1, pp. 519–528, Jan. 2014.

[34] P. Knippertz *et al.*, "The possible role of local air pollution in climate change in West Africa," *Nature Clim. Change*, vol. 5, no. 9, pp. 815–822, Aug. 2015.

[35] Z. Zhu, S. Wang, and C. E. Woodcock, "Improvement and expansion of the Fmask algorithm: Cloud, cloud shadow, and snow detection for Landsats 4–7, 8, and Sentinel 2 images," *Remote Sens. Environ.*, vol. 159, pp. 269–277, Mar. 2015.

Dong Yan received the B.S. degree in geographic information systems from Sichuan Normal University, Chengdu, China, in 2006, the M.S. degree in geography from the Institute of Mountain Hazards and Environment, Chinese Academy of Sciences, Chengdu, China, in 2009, and the Ph.D. degree in geography from the University of Oklahoma, Norman, OK, USA, in 2014.

He is currently a Postdoctoral Fellow with the Geospatial Sciences Center of Excellence, South Dakota State University, Brookings, SD, USA. His research focuses on investigating the long-term changes in rainforest phenology using observations acquired by geostationary satellites.

Mr. Yan is a member of the American Geophysical Union and a recipient of the Graduate Research Award from the University of Oklahoma in 2013.

Xiaoyang Zhang received the B.S. degree in geography from Peking University, Beijing, China, in 1984, the M.S. degree in geography from the Nanjing Institute of Geography and Limnology, Chinese Academy of Sciences, Nanjing, China, in 1991, and the Ph.D. degree in geography from King's College London, University of London, London, U.K., in 1999.

He is currently a Senior Scientist with the Geospatial Sciences Center of Excellence at South Dakota State University (SDSU), Brookings, SD, USA. Prior to joining SDSU in 2013, he was a Research Assistant Professor with Boston University, Boston, MA, USA, and a Senior Research Scientist in Earth Resources Technology at the National Oceanic and Atmospheric Administration (NOAA), National Environmental Satellite, Data, and Information Service, Center for Satellite Applications and Research (STAR), Camp Spring, MD, USA. His research focuses on land surface dynamics, biomass burning emissions, land cover and land use change, and climate-terrestrial ecosystem interaction with research funding from NASA and NOAA.

Dr. Zhang is a member of the American Geophysical Union, the Association of American Geographers, and the International Association of Wildland Fire.

Yunyue Yu received the B.S. degree in physics from the Ocean University of China, Qingdao, China, in 1982, the M.S. degree in advanced physics from Peking University, Beijing, China, in 1986, and the Ph.D. degree in aerospace engineering science from the University of Colorado, Boulder, CO, USA, in 1996.

He is currently a Physical Scientist at the National Oceanic and Atmospheric Administration, National Environmental Satellite, Data, and Information Service, Center for Satellite Applications and Research (STAR), Camp Springs, MD, USA. His research focuses on land surface temperature and albedo retrievals from remote sensing.

Wei Guo received the M.S. degree in satellite meteorology from Peking University, Beijing, China, in 1990.

He is currently a Senior Scientific/System Programmer at the I. M. Systems Group, Inc., National Oceanic and Atmospheric Administration, National Environmental Satellite, Data, and Information Service, College Park, MD, USA. His work focuses on the research and development of software to support the remote sensing of terrestrial ecosystems.